

Numerical Study of Quantum Resonances in Chaotic Scattering

Kevin K. Lin*

Abstract

This paper presents numerical evidence that for quantum systems with chaotic classical dynamics, the number of scattering resonances near an energy E scales like $\hbar^{-\frac{D(K_E)+1}{2}}$ as $\hbar \rightarrow 0$. Here, K_E denotes the subset of the classical energy surface $\{H = E\}$ which stays bounded for all time under the flow generated by the Hamiltonian H and $D(K_E)$ denotes its fractal dimension. Since the number of bound states in a quantum system with n degrees of freedom scales like \hbar^{-n} , this suggests that the quantity $\frac{D(K_E)+1}{2}$ represents the effective number of degrees of freedom in scattering problems.

1 Introduction

Quantum mechanics identifies the energies of stationary states in an isolated physical system with the eigenvalues of its Hamiltonian operator. Because of this, eigenvalues play a central role in the study of bound states, such as those describing the electronic structures of atoms and molecules.¹ When the corresponding classical system allows escape to infinity, resonances replace eigenvalues as fundamental quantities: The presence of a resonance at $\lambda = E - i\gamma$, with E real and $\gamma > 0$, gives rise to a dissipative metastable state with energy E and decay rate γ , as described in [37]. Such states are essential in scattering theory.²

An important property of eigenvalues is that one can count them using only the classical Hamiltonian function $H(x, p) = \frac{1}{2}||p||^2 + V(x)$ and Planck's constant \hbar : For fixed energies $E_0 < E_1$, the number $N_{eig}(E_0, E_1, \hbar)$ of

*Department of Mathematics, University of California, Berkeley, CA 94720. E-mail: kkylin@math.berkeley.edu. The author is supported by a fellowship from the Fannie and John Hertz Foundation.

¹For examples, see [5].

²Systems which are not effectively isolated but interact only weakly with their environment can also exhibit resonant behavior. For example, electronic states of an “isolated” hydrogen atom are eigenfunctions of a self-adjoint operator, but coupling the electron to the radiation field turns those eigenstates into metastable states with finite lifetimes. This paper does not deal with dissipative systems and is only concerned with scattering.

eigenvalues in $[E_0, E_1]$ is

$$N_{eig}(E_0, E_1, \hbar) \approx \frac{\text{vol}(\{E_0 \leq H \leq E_1\})}{(2\pi\hbar)^n}, \quad (1)$$

where n denotes the number of degrees of freedom and $\text{vol}(\cdot)$ phase space volume. This result, known as the *Weyl law*, expresses the density of quantum states using the classical Hamiltonian function.³ No direct generalization to resonances is currently known.

In this paper, numerical evidence for a Weyl-like power law is presented for resonances in a two-dimensional model with three symmetrically-placed gaussian potentials. A conjecture, based on the work of Sjöstrand [27] and Zworski [35], states that the number of resonances $\lambda = E - i\gamma$ with $E_0 < E < E_1$ and $0 < \gamma < \hbar$ asymptotically lies between $C_1 \hbar^{-\frac{D(K_{E_1})+1}{2}}$ and $C_0 \hbar^{-\frac{D(K_{E_0})+1}{2}}$ as $\hbar \rightarrow 0$, where

$$\begin{aligned} D(\cdot) &= \text{dimension (see below)}, \\ K_E &= K \cap \{H = E\}, \\ K &= \{(x, p) : \sup_t \|\Phi_t(x, p)\| < \infty\}, \\ \Phi_t &= \text{flow generated by } H. \end{aligned} \quad (2)$$

If $D(K_E)$ depends continuously on E and $|E_1 - E_0|$ is sufficiently small, then $D(K_{E_1}) \approx D(K_{E_0})$ and the number of resonances in such a region is comparable to $\hbar^{-\frac{D(K_E)+1}{2}}$ for any $E \in [E_0, E_1]$.

The sets K and K_E are *trapped sets* and consist of initial conditions which generate trajectories that stay bounded forever. In systems where $\{H \leq E\}$ is bounded for all E , the conjecture reduces to the Weyl asymptotic \hbar^{-n} .

The notion of dimension requires some comment: The “triple gaussian” model considered here has very few trapped trajectories, and K and K_E (for any energy E) have vanishing Lebesgue measures. Thus, $D(K)$ is strictly less than $2n = 4$ and $D(K_E) < 2n - 1 = 3$. In fact, the sets K and K_E are fractal, as are trapped sets in many other chaotic scattering problems. Also, in this paper, the term “chaotic” always means *hyperbolic*; see Sjöstrand [27] or Gaspard [12] for definitions.

³For a beautiful exposition of early work on this and related themes, see [16]. For recent work in the semiclassical context, see [7].

This paper is organized as follows: First, the model system is defined. This is followed by mathematical background information, as well as a heuristic argument for the conjecture. Then, numerical methods for computing resonances and fractal dimensions are developed, and numerical results are presented and compared with known theoretical predictions.

Notation. In this paper, H denotes the Hamiltonian function $\frac{1}{2}||p||^2 + V(x)$ and \widehat{H} the corresponding Hamiltonian operator $-\frac{\hbar^2}{2}\Delta + V(x)$, where $\Delta = \sum_{k=1}^n \frac{\partial^2}{\partial x_k^2}$ is the usual Laplacian and V acts by multiplication.

2 Triple Gaussian Model

The model system has $n = 2$ degrees of freedom; its phase space is R^4 , whose points are denoted by (x, y, p_x, p_y) .

First, it is convenient to define

$$G_{x_0}^\sigma(x) = \exp\left(-\frac{(x - x_0)^2}{2\sigma^2}\right). \quad (3)$$

Similarly, put

$$\begin{aligned} G_{(x_0, y_0)}^\sigma(x, y) &= (G_{x_0}^\sigma \otimes G_{y_0}^\sigma)(x, y) \\ &= G_{x_0}^\sigma(x) \cdot G_{y_0}^\sigma(y) \end{aligned} \quad (4)$$

in two dimensions.

Now, define H by

$$H(x, y, p_x, p_y) = \frac{1}{2}(p_x^2 + p_y^2) + V_3(x, y) \quad (5)$$

where the potential V_m is given by

$$\begin{aligned} V_m &= \sum_{k=1}^m G_{c(k, m)}^\sigma, \\ c(k, m) &= (R \cos(\frac{2\pi k}{m}), R \sin(\frac{2\pi k}{m})). \end{aligned} \quad (6)$$

That is, it consists of m gaussian “bumps” placed at the vertices of a regular m -gon centered at the origin, at a distance $R > 0$ from the origin. This paper focuses on the case $m = 3$ because it is the simplest case that exhibits nontrivial dynamics in two dimensions. However, the case $m = 2$ is also relevant because it is well-understood: See Miller [21] for early heuristic results and Gérard and Sjöstrand [13] for a rigorous treatment. Thus, double gaussian scattering serves as a useful test case for the techniques described here.

The quantized Hamiltonian \widehat{H} is similarly defined:

$$\widehat{H} = -\frac{\hbar^2}{2}\Delta + V_3. \quad (7)$$

See Figure 1.

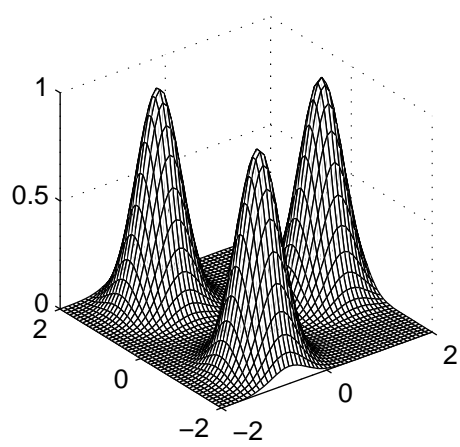


Figure 1: Triple gaussian potential

3 Background

This section provides a general discussion of resonances and motivates the conjecture in the context of the triple gaussian model. However, the notation reflects the fact that most of the definitions and arguments here carry over to more general systems with n degrees of freedom. The reader should keep in mind that $n = 2$ for the triple gaussian model.

There exists an extensive literature on resonances and semiclassical asymptotics in other settings. For example, see [9, 10, 11, 34] for detailed studies of the classical and quantum mechanics of hard disc scattering.

3.1 Resonances

Resonances can be defined mathematically as follows: Set $R(z) = (\widehat{H} - zI)^{-1}$ for real z , where I is the identity operator. This one-parameter family of operators $R(z)$ is the *resolvent* and is meromorphic with suitable modifications of its domain and range. The poles of its continuation into the complex plane are, by definition, the *resonances* of \widehat{H} .⁴

Less abstractly, resonances are generalized eigenvalues of \widehat{H} . Thus, we should solve the time-independent Schrödinger equation

$$\widehat{H}\psi = \lambda\psi \quad (8)$$

to obtain the resonance λ and its generalized eigenfunction ψ . In bound state computations, one approximates ψ as a finite linear combination of basis functions and solves a finite-dimensional version of the equation above.

⁴For more details and some references, see [37].

To carry out similar calculations for resonances, it is necessary that ψ lie in a function space which facilitates such approximations, for example L^2 .

Let ψ and λ solve (8). Then $e^{-\frac{i}{\hbar}\lambda t} \cdot \psi$ solves the time-dependent Schrödinger equation

$$i\hbar \frac{\partial \psi}{\partial t} = \hat{H}\psi. \quad (9)$$

It follows that $\text{Im}(\lambda)$ must be negative because metastable states decay in time. Now suppose, for simplicity, that $n = 1$.⁵ Then solutions of (8) with energy E behave like $e^{-\frac{i}{\hbar}\sqrt{2E}x}$ for large $x > 0$. Substituting $\lambda = E - i\gamma$ for E yields $e^{-\frac{i}{\hbar}\sqrt{2\lambda}x}$, which grows exponentially because $\text{Im}(\sqrt{E - i\gamma}) < 0$. Thus, finite rank approximations of \hat{H} cannot capture such generalized eigenfunctions. However, if we make the formal substitution $x \mapsto xe^{i\alpha}$, then the wave function becomes $\exp\left(-\frac{i}{\hbar}\sqrt{2\lambda} \cdot e^{i\alpha} \cdot x\right)$. Choosing $\alpha > \frac{1}{2}\tan^{-1}(\gamma/E)$ forces ψ to decay exponentially.

This procedure, called *complex scaling*, transforms the Hamiltonian operator \hat{H} into the *scaled operator* \hat{H}_α . It also maps metastable states ψ with decay rate $\gamma < E \tan(2\alpha)$ to genuine L^2 eigenfunctions ψ_α of \hat{H}_α . The corresponding resonance λ becomes a genuine eigenvalue: $\hat{H}_\alpha \psi_\alpha = \lambda \psi_\alpha$. Furthermore, resonances of \hat{H} will be invariant under small perturbations in α , whereas other eigenvalues of \hat{H}_α will not. The condition $\alpha > \frac{1}{2}\tan^{-1}(\gamma/E)$ implies that, for small γ and fixed E , the method will capture a resonance $\lambda = E - i\gamma$ if and only if $\gamma < 2E\alpha + O(\alpha^2)$. We can perform complex scaling in higher dimensions by substituting $r \mapsto re^{i\alpha}$ in polar coordinates.

In algorithmic terms, this means we can compute eigenvalues of \hat{H}_α for a few different values of α and look for invariant values, as demonstrated in Figure 2. In addition to its accuracy and flexibility, this is one of the advantages of complex scaling: The invariance of resonances under perturbations in α provides an easy way to check the accuracy of calculations, mitigating some of the uncertainties inherent in computational work.⁶ Note that the scaled operator \hat{H}_α is no longer self-adjoint, which results in non-hermitian finite-rank approximations and complex eigenvalues.

This method, first introduced for theoretical purposes by Aguilar and Combes [1] and Balslev and Combes [3], was further developed by B. Simon in [26]. It has since become one of the main tools for computing resonances in physical chemistry [22, 31, 32, 24]. For recent mathematical progress, see [18, 27, 28] and references therein.

⁵The analysis in higher dimensions requires some care, but the essential result is the same.

⁶For a different approach to computing resonances, see [33] and the references there.

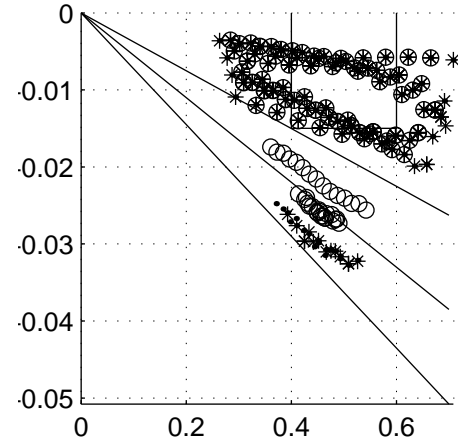


Figure 2: Illustration of complex scaling: The three lines indicate the location of the rotated continuous spectrum for different values of α , while the box at the top of the figure is the region in which resonances are counted. Eigenvalues which belong to different values of α are marked with different styles of points. As explained later, only eigenvalues near the region of interest are computed. This results in a seemingly empty plot.

For reference, the scaled triple-gaussian operator \hat{H}_α is

$$\hat{H}_\alpha = -e^{-2i\alpha} \cdot \frac{\hbar^2}{2} \Delta + V_{3,\alpha}, \quad (10)$$

where

$$\begin{aligned} V_{m,\alpha} &= \sum_{k=1}^m G_{c_\alpha(k,m)}^{\sigma_\alpha}, \\ \sigma_\alpha &= e^{-i\alpha} \cdot \sigma, \\ c_\alpha(k,m) &= e^{-i\alpha} c(k,m). \end{aligned} \quad (11)$$

Note that these expressions only make sense because $G_{x_0}^\sigma(x)$ is analytic in x , x_0 , and σ .

3.2 Fractal Dimension

Recall that the *Minkowski dimension* of a given set $U \subset \mathbb{R}^m$ is

$$D = \inf \left\{ d : \limsup_{\epsilon \rightarrow 0} (\epsilon^{d-m} \cdot \text{vol}(U_\epsilon)) < \infty \right\}, \quad (12)$$

where $U_\epsilon = \{y \in \mathbb{R}^m : \text{dist}(y, U) < \epsilon\}$. A simple calculation yields

$$D(U) = \lim_{\epsilon \rightarrow 0} \frac{\log(\text{vol}(U_\epsilon)/\epsilon^m)}{\log(1/\epsilon)} \quad (13)$$

if the limit exists.

Texts on the theory of dimensions typically begin with the Hausdorff dimension because it has many desirable properties. In contrast, the Minkowski dimension can be somewhat awkward: For example, a countable union of zero-dimensional sets (points) can have positive Minkowski dimension. But, the Minkowski dimension is sometimes easier to manipulate and almost always easier to compute. It also arises in the heuristic argument given below.

For a detailed treatment of different definitions of dimension and their applications in the study of dynamical systems, see [8, 23].

3.3 Generalizing the Weyl Law

The formula

$$\frac{\text{vol}(\{E_0 \leq H \leq E_1\})}{(2\pi\hbar)^n} \quad (14)$$

makes no sense in scattering problems because the volume on the right hand side is infinite for most choices of E_0 and E_1 , and this seems to mean that there is no generalization of the Weyl law in the setting of scattering theory. However, the following heuristic argument suggests otherwise:

As mentioned before, a metastable state corresponding to a resonance $\lambda = E - i\gamma$ has a time-dependent factor of the form $e^{-\frac{i}{\hbar}\lambda t} = e^{-\frac{i}{\hbar}Et} \cdot e^{-\frac{\gamma}{\hbar}t}$. A wave packet whose dynamics is dominated by λ (and other resonances near it) would therefore exhibit temporal oscillations of frequency $O(E/\hbar)$ and lifetime $O(\hbar/\gamma)$. Heuristically, then, the number of times the particle “bounces” in the “trapping region”⁷ before escaping should be comparable to $\frac{E}{\hbar} \cdot \frac{\hbar}{\gamma} = \frac{E}{\gamma}$.

In the semiclassical limit, the dynamics of the wave packet should be well-approximated by a classical trajectory. Let $T(x, y, p_x, p_y)$ denote the time for the particle to escape the system starting at position (x, y) with momentum (p_x, p_y) . The diameter of the trapping region is $O(R)$, and typical velocities in the energy surface $\{H = E\}$ are $O(\sqrt{E})$ (mass set to unity), so the number of times a classical particle bounces before escaping should be $O(T\sqrt{E}/R)$. This suggests that, in the limit $\hbar \rightarrow 0$, $T\sqrt{E}/R \sim E/\gamma$ and consequently

$$T \sim \frac{R\sqrt{E}}{\gamma}. \quad (15)$$

Fix $\gamma_0 > 0$, and consider

$$N_{\text{res}} = \#\{E - i\gamma : E_0 \leq E \leq E_1, \gamma \leq \gamma_0\} \quad (16)$$

⁷For our triple gaussian system, that would be the triangular region bounded by the gaussian bumps.

for fixed energies E_0 and E_1 : Equation (15) implies that $T \geq R\sqrt{E_0}/\gamma_0$, so by analogy with the Weyl law,

$$\frac{\text{vol}(\{E_0 \leq H \leq E_1, T \geq \frac{R\sqrt{E_0}}{\gamma_0}\})}{(2\pi\hbar)^n} \quad (17)$$

follows as an approximation for the number of quantum states with the specified energies and decay rates.

Now, the function $1/T$ is nonnegative for all (x, y, p_x, p_y) and vanishes on $K_{[E_0, E_1]} = K \cap \{E_0 \leq H \leq E_1\}$. Assuming that $1/T$ is sufficiently regular,⁸ this suggests

$$1/T(x, y, p_x, p_y) \sim d_{K_{[E_0, E_1]}}(x, y, p_x, p_y)^2, \quad (18)$$

where $d_{K_{[E_0, E_1]}}$ denotes distance to $K_{[E_0, E_1]}$. It follows that N_{res} should scale like

$$\frac{\text{vol}(\{E_0 \leq H \leq E_1, d_{K_{[E_0, E_1]}} \leq \gamma_0^{\frac{1}{2}}\})}{\hbar^n}. \quad (19)$$

For small γ_0 , this becomes

$$C(R, E_0, E_1) \cdot \hbar^{-n} \cdot \gamma_0^{\frac{2n-D(K_{[E_0, E_1]})}{2}} \quad (20)$$

for some constant C , by (12). Choosing $\gamma_0 = \hbar$ and assuming that $D(K_E)$ decreases monotonically with increasing E (as is the case in Figure 22), we obtain

$$C_1 \hbar^{-\frac{D(K_{E_1})+1}{2}} \leq N_{\text{res}} \leq C_0 \hbar^{-\frac{D(K_{E_0})+1}{2}}. \quad (21)$$

If $|E_1 - E_0|$ is sufficiently small, then $D(K_{[E_0, E_1]}) \approx D(K_E) + 1$ for $E \in [E_0, E_1]$, and

$$N_{\text{res}} \sim \hbar^{-\frac{D(K_E)+1}{2}}. \quad (22)$$

In [27], Sjöstrand proved the following rigorous upper bound: For $\gamma_0 > 0$ satisfying $C\hbar < \gamma_0 < 1/C$,

$$N_{\text{res}} = O\left(C_\delta \hbar^{-n} \gamma_0^{\frac{2n-D(K_{[E_0, E_1]})+\delta}{2}}\right) \quad (23)$$

holds for all $\delta > 0$. When the trapped set is of *pure dimension*, that is when the infimum in Equation (12) is achieved, one can take $\delta = 0$. Setting $\gamma_0 = \hbar$ gives an upper bound of the form (22).

⁸In fact, this is numerically self-consistent: Assume that $1/T$ vanishes to order ν (with ν not necessarily equal to 2) on K , and assume the conjecture. Then the number of resonances would scale like $\hbar^{(2n-D(K))/\nu}$, from which one can solve for ν . With the numerical data we have, this indeed turns out to be 2 (but with significant fluctuations).

Also, if $1/T$ does not vanish quadratically *everywhere* on K , variations in its regularity may affect the correspondence between classical trapping and the distribution of resonances.

In his proof, Sjöstrand used the semiclassical argument above with escape functions and the Weyl inequality for singular values. Zworski continued this work in [35], where he proved a similar result for scattering on convex co-compact hyperbolic surfaces with no cusps. His work was motivated by the availability of a large class of examples with hyperbolic flows, easily computable dimensions, and the hope that the Selberg trace formula could help obtain lower bounds. But, these hopes remain unfulfilled so far [14], and that partly motivates this work.

4 Computing Resonances

Complex scaling reduces the problem of calculating resonances to one of computing eigenvalues. What remains is to approximate the operator \widehat{H}_α by a rank N operator $\widehat{H}_{N,\alpha}$ and to develop appropriate numerical methods. For comparison, see [22, 31, 32, 24] for applications of complex scaling to problems in physical chemistry.

4.1 Choice of Scaling Angle.

One important consideration in resonance computation is the choice of the scaling angle α : Since we are interested in counting resonances in a box $[E_0, E_1] - i[0, \hbar]$, it is necessary to choose $\alpha \geq \tan^{-1}\left(\frac{\hbar}{E_0}\right)$ so that the continuous spectrum of \widehat{H}_α is shifted out of the box $[E_0, E_1] - i[0, \hbar]$ (see Figure 2).

In fact, the resonance calculation uses

$$\begin{aligned} \alpha &= \tan^{-1}\left(\frac{\hbar}{E_0}\right) \\ &= \frac{\hbar}{E_0} + O(\hbar^2). \end{aligned} \quad (24)$$

This choice of α helps avoid the *pseudospectrum* [30, 36]:

Let A be an $N \times N$ matrix, and let $R(z)$ be the resolvent $(A - zI)^{-1}$. It is well known that when A is *normal*, that is when A commutes with its adjoint A^* , the spectral theorem applies and the inequality

$$\begin{aligned} \|R(z)\| &= \|(A - zI)^{-1}\| \\ &\leq \text{dist}(z, \sigma(A))^{-1} \end{aligned} \quad (25)$$

holds ($\sigma(A)$ denotes the spectrum of A). When A is not normal, no such inequality holds and $\|R(z)\|$ can become very large for z far from $\sigma(A)$. This leads one to define ϵ -*pseudospectrum*:

$$\Lambda_\epsilon(A) = \{z : \|R(z)\| \geq 1/\epsilon\}. \quad (26)$$

Using the fact that A is a matrix, one can show that $\Lambda_\epsilon(A)$ is equal to the set

$$\{z : \exists A' \text{ such that } z \in \sigma(A + A'), \|A'\| \leq \epsilon\}. \quad (27)$$

That is, the ϵ -pseudospectrum of A consists of those complex numbers z which are eigenvalues of an ϵ -perturbation of A .

The idea of pseudospectrum can be extended to general linear operators. In [30], it is emphasized that for non-normal operators, the pseudospectrum can create “false eigenvalues” which make the accurate numerical computation of eigenvalues difficult. In [36], this phenomenon is explained using semiclassical asymptotics. Roughly speaking, the pseudospectrum of the scaled operator \widehat{H}_α is given by the closure of

$$\{z : z = H_\alpha(x, y, p_x, p_y)\} \quad (28)$$

of its *symbol* H_α , which is the scaled Hamiltonian function

$$H_\alpha(x, y, p_x, p_y) = e^{-2i\alpha} \cdot \frac{p_x^2 + p_y^2}{2} + V_{3,\alpha} \quad (29)$$

in this case. Choosing α to be comparable to \hbar ensures that the imaginary part of H_α is also comparable to \hbar , which keeps the pseudospectrum away from the counting box $[E_0, E_1] - i[0, \hbar]$; a larger α would contribute a larger α^2 term to the imaginary part of H_α and enlarge the pseudospectrum. As one can see in Figures 31 - 34, the invariance of resonances under perturbations in α also helps filter out pseudospectral effects.

This consideration also points out the *necessity* of the choice $\alpha = \tan^{-1}\left(\frac{\hbar}{E_0}\right)$: To avoid pseudospectral effects, α must be $O(\hbar)$. On the other hand, if $\alpha = o(\hbar)$, then finite rank approximations may fail to capture resonances in the region of interest.

4.2 Eigenvalue Computation

Suppose that we have constructed $\widehat{H}_{N,\alpha}$. In the case of eigenvalues, the Weyl law states that $N_{eig} = O(\hbar^{-2})$ as $\hbar \rightarrow 0$, since our system has $n = 2$ degrees of freedom. Thus, in order to capture a sufficient number of eigenvalues, the rank N of the matrix approximation must scale like \hbar^{-2} . In the absence of more detailed information on the density of resonances, the resonance computation requires a similar assumption to ensure sufficient numerical resolution.

Thus, for moderately small \hbar , the matrix has $N^2 \sim \hbar^{-4}$ entries, which rapidly becomes prohibitive on most computers available today. Furthermore, even if one does not store the entire matrix, numerical packages like LAPACK [2] require $O(N^2)$ auxiliary storage, again making practical calculations impossible.

Instead of solving the eigenvalue problem $\widehat{H}_{N,\alpha}v = \lambda v$ directly, one solves the equivalent eigenvalue problem

$$\left(\widehat{H}_{N,\alpha} - \lambda_0\right)^{-1} v = \lambda' v. \quad (30)$$

Efficient implementations of the Arnoldi algorithm [19] can solve for the largest few eigenvalues λ' of $(\widehat{H}_{N,\alpha} - \lambda_0)^{-1}$. But $\lambda = \lambda_0 + 1/\lambda'$, so this method allows one to compute a subset of the spectrum of $\widehat{H}_{N,\alpha}$ near a given λ_0 .

Such algorithms require a method for applying the matrix $(\widehat{H}_{N,\alpha} - \lambda_0)^{-1}$ to a given vector v at each iteration step. In the resonance computation, this is done by solving $(\widehat{H}_{N,\alpha} - \lambda_0)w = v$ for w by applying conjugate gradient to the normal equations (see [4]).⁹ The resonance program, therefore, consists of two nested iterative methods: An outer Arnoldi loop and an inner iterative linear solver for $(\widehat{H}_{N,\alpha} - \lambda_0)w = v$. This computation uses ARPACK¹⁰, which provides a flexible and efficient implementation of the Arnoldi method.

To compute resonances near a given energy E , the program uses $\lambda_0 = E + ia$, $a > 0$, instead of $\lambda_0 = E$: This helps control the condition number of $\widehat{H}_{N,\alpha} - \lambda_0$ and gives better error estimates and convergence criteria.¹¹

4.3 Matrix Representations

4.3.1 Choice of Basis

While one can discretize the differential operator \widehat{H}_α via finite differences, in practice it is better to represent the operator using a basis for a subspace of the Hilbert space L^2 : This should better represent the properties of wave functions near infinity and obtain smaller (but more dense) matrices.

Common basis choices in the chemical literature include so-called “phase space gaussian” [6] and “distributed gaussian” bases [15]. These bases are not orthogonal with respect to the usual L^2 inner product, so one must explicitly orthonormalize the basis before computing the matrix representation of \widehat{H}_α . In addition to the computational cost, this also requires storing the entire matrix and severely limits the size of the problem one can

⁹That is, instead of solving $Aw = v$, one solves $A^*Aw = A^*v$. This is necessary because $\widehat{H}_{N,\alpha}$ is non-hermitian, and conjugate gradient only works for positive definite matrices. This is not the best numerical method for non-hermitian problems, but it is easy to implement and suffices in this case.

¹⁰See [19] for details on the package, as well as an overview of Krylov subspace methods.

¹¹Most of the error in solving the matrix equation $(\widehat{H}_{N,\alpha} - \lambda_0)w = v$ concentrates on eigenspaces of $(\widehat{H}_{N,\alpha} - \lambda_0)^{-1}$ with large eigenvalues. These are precisely the desired eigenvalues, so in principle one can tolerate inaccurate solutions. However, the calculation requires convergence criteria and error estimates for the linear solver, and using $a > 0$, say $a = 1$, turns out to ensure a relative error of about 10^{-6} after about 17-20 iterations of the conjugate gradient solver. Since we only wanted to count eigenvalues, a more accurate (and expensive) computation of resonances was not necessary.

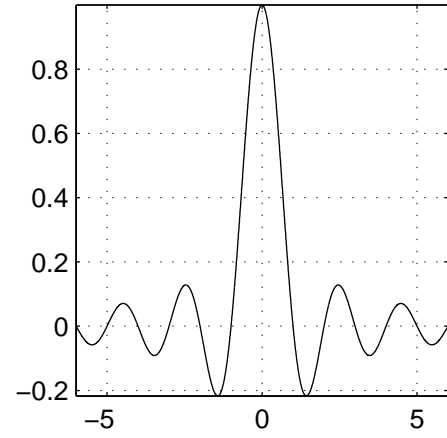


Figure 3: A sinc function with $m = 0$, $\Delta x = 1$.

solve. Instead, this computation uses a *discrete-variable representation* (DVR) basis [20]:

Consider, for the moment, the one dimensional problem of finding a basis for a “good” subspace of $L^2(R)$. Fix a constant $\Delta x > 0$, and for each integer m , define

$$\phi_{m,\Delta x}(x) = \sqrt{\Delta x} \cdot \frac{\sin\left(\frac{\pi}{\Delta x}(x - m\Delta x)\right)}{\pi(x - m\Delta x)}. \quad (31)$$

(This is known as a “sinc” function in engineering literature [25]. See Figure 3.) The Fourier transform of $\phi_{m,\Delta x}$ is

$$\widehat{\phi}_{m,\Delta x}(\omega) = \begin{cases} e^{-im\Delta x} \cdot \sqrt{\Delta x}, & |\omega| \leq \pi/\Delta x \\ 0, & |\omega| > \pi/\Delta x \end{cases} \quad (32)$$

One can easily verify that $\{\phi_{m,\Delta x}\}$ forms an orthonormal basis for the closed subspace of L^2 functions whose Fourier transforms are supported in $[-\pi/\Delta x, \pi/\Delta x]$.

To find a basis for corresponding space of band-limited functions in $L^2(R^2)$, simply form the tensor products

$$\phi_{mn}(x_0, y_0) = \phi_{m,\Delta x}(x_0)\phi_{n,\Delta y}(y_0). \quad (33)$$

The basis has a natural one-to-one correspondence with points $(m\Delta_1 + X_0, n\Delta_2 + Y_0)$ on a regular lattice of grid points in a box $[X_0, X_1] \times [Y_0, Y_1]$ covering the spatial region of interest. (See Figure 4.) Using this basis, it is easy to compute matrix elements for \widehat{H}_α .

4.3.2 Tensor Product Structure

An additional improvement comes from the separability of the Hamiltonian: Each term in the scaled Hamiltonian

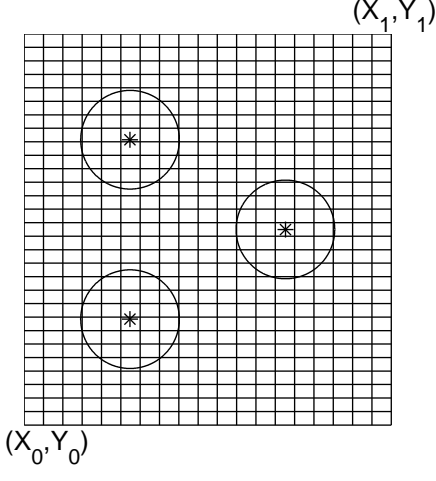


Figure 4: Illustration of resonance program parameters in configuration space: The lower-left corner of the mesh is (X_0, Y_0) , while the upper right corner is (X_1, Y_1) . The mesh contains $N_x \times N_y$ grid points, and a basis function ϕ_{mn} is placed at each grid point. Stars mark the centers of the potentials, the circles have radius 2σ (with $\sigma = 1/3$), and R is set to 1.4. Parameters for the classical computation are depicted in Figure 5.

\hat{H}_α splits into a tensor product:

$$\frac{\partial^2}{\partial x^2} = \frac{d^2}{dx^2} \otimes I_y \quad (34)$$

$$\frac{\partial^2}{\partial y^2} = I_x \otimes \frac{d^2}{dy^2} \quad (35)$$

$$G_{(x_0, y_0)}^\sigma = G_{x_0}^\sigma \otimes G_{y_0}^\sigma, \quad (36)$$

where I_x and I_y denote identity operators on copies of $L^2(R)$. Since the basis $\{\phi_{mn}\}$ consists of tensor products of one dimensional bases, $\hat{H}_{N,\alpha}$ is also a short sum of tensor products. Thus, if we let N_x denote the number of grid points in the x direction and let N_y denote the number of grid points in the y direction, then $N = N_x \cdot N_y$ and $\hat{H}_{N,\alpha}$ is a sum of five matrices of the form $A_x \otimes A_y$, where A_x is $N_x \times N_x$ and A_y is $N_y \times N_y$.

Such tensor products of matrices can be applied to arbitrary vectors efficiently using the outer product representation.¹² Since the rank of $\hat{H}_{N,\alpha}$ is $N = N_x \cdot N_y$ and $N_x \approx N_y$ in these computations, we can store the tensor factors of the matrix $\hat{H}_{N,\alpha}$ using $O(N)$ storage instead of $O(N^2)$, and apply $\hat{H}_{N,\alpha}$ to a vector in $O(N^{3/2})$ time instead of $O(N^3)$. The resulting matrix is not sparse, as

¹²The tensor product of two column vectors v and w can be represented as $v \cdot w^T$. We then have $(A \otimes B) \cdot (v \otimes w) = (Av) \cdot (Bw)^T$, which extends by linearity to $(A \otimes B) \cdot u = A \cdot u \cdot B^T$.

one can see from the matrix elements for the Laplacian below.

Note that this basis fails to take advantage of the discrete rotational symmetry of the triple gaussian Hamiltonian. Nevertheless, the tensor decomposition provides sufficient compression of information to facilitate efficient computation.

4.3.3 Matrix Elements

It is straightforward to calculate matrix elements for the Laplacian on R^1 :

$$K_{mn} = \begin{cases} \frac{\hbar^2 \pi^2}{\Delta x^2}, & m = n \\ (-1)^{m-n} \cdot \frac{\hbar^2}{\Delta x^2 \cdot (m-n)^2}, & m \neq n \end{cases} \quad (37)$$

There is no closed form expression for the matrix elements of the potential, but it is easy to perform numerical quadrature with these functions. For example, to compute

$$V_{mn} = \int G(x) \phi_m(x) \phi_n(x) dx \quad (38)$$

for $G(x) = e^{-\frac{x^2}{2\sigma^2}}$, one computes

$$V_{mn} \approx \sum_{k=-N}^N G(k\delta) \cdot \delta \cdot \phi_m(k\delta) \cdot \phi_n(k\delta), \quad (39)$$

where the stepsize δ should satisfy $\delta \leq \Delta x/2$. It is easy to show that the error is bounded by the sum of

$$2 \exp\left(-\frac{|\sigma|^2 \pi^2}{2\delta^2}\right), \quad (40)$$

which controls the *aliasing error*, and

$$\frac{\sqrt{2\pi |\sigma|^2}}{\Delta x} \exp\left(-\frac{(N-1)^2 \delta^2}{2|\sigma|^2}\right). \quad (41)$$

which controls the *truncation error*.

4.3.4 Other Program Parameters

The grid spacing Δx implies a limit on the maximum possible momentum in a wave packet formed by this basis. In order to obtain a finite-rank operator, it is also necessary to limit the number of basis functions.

The resonance computation used the following parameters:

1. X_0, X_1, Y_0 , and Y_1 are chosen to cover the region of the configuration space for which $V_3(x, y) \geq 10^{-4}$.

2. Let $L_x = X_1 - X_0$ and $L_y = Y_1 - Y_0$ denote the dimension of the computational domain. The resonance calculation uses $N = N_x \cdot N_y$ basis functions, with $N_x = 1.6 \cdot \frac{L_x \sqrt{8E}}{2\pi\hbar}$ and $N_y = 1.6 \cdot \frac{L_y \sqrt{8E}}{2\pi\hbar}$.

3. This gives

$$\begin{aligned}\Delta x &= L_x/N_x, \\ \Delta y &= L_y/N_y,\end{aligned}\quad (42)$$

which limits the maximum momentum in a wave packet to $|p_x| \leq \pi\hbar/\Delta x = 1.6\sqrt{2E}$ and $|p_y| \leq \pi\hbar/\Delta y = 1.6\sqrt{2E}$.

5 Trapped Set Structure

5.1 Poincaré Section

Because the phase space for the triple gaussian model is R^4 and its flow is chaotic, a direct computation of the trapped set dimension is difficult. Instead, we try to compute its intersection with a *Poincaré section*:

Let E be a fixed energy, and recall that R is the distance from each gaussian bump to the origin. Choose $R_0 < R$ so that the circles C_k of radius R_0 centered at each potential, for $k = 0, 1, 2$, do not intersect. The angular momentum p_θ with respect to the k th potential center is defined by $p_\theta = \Delta x \cdot p_y - \Delta y \cdot p_x$, where $\Delta x = x - R \cos(\theta_k)$, $\Delta y = y - R \sin(\theta_k)$, and $\theta_k = \frac{2\pi k}{3}$.

Let P be the submanifold $P_0 \cup P_1 \cup P_2$ of R^4 (see Figure 5), where the coordinates (θ, p_θ) in the submanifold P_k are related to ambient phase space coordinates (x, y, p_x, p_y) by

$$\begin{aligned}x &= R \cos(\theta_k) + R_0 \cos(\theta + \theta_k), \\ y &= R \sin(\theta_k) + R_0 \sin(\theta + \theta_k), \\ p_x &= p_r \cos(\theta + \theta_k) - \frac{p_\theta}{R_0} \sin(\theta + \theta_k), \\ p_y &= p_r \sin(\theta + \theta_k) + \frac{p_\theta}{R_0} \cos(\theta + \theta_k)\end{aligned}\quad (43)$$

and the radial momentum p_r is

$$p_r = \sqrt{E - V_3(x, y) - \frac{p_\theta^2}{2R_0^2}}. \quad (44)$$

Note that this implicitly embeds P into the energy surface $\{H = E\}$, and the radial momentum p_r is always positive: The vector (p_x, p_y) points away from the center of C_k .

The trapped set is naturally partitioned into two subsets: The first consists of trajectories which visit all three bumps, the second of trajectories which bounce between two bumps. The second set forms a one-dimensional subspace of K_E , so the *finite stability* of the Minkowski dimension¹³ implies that the second set does not contribute

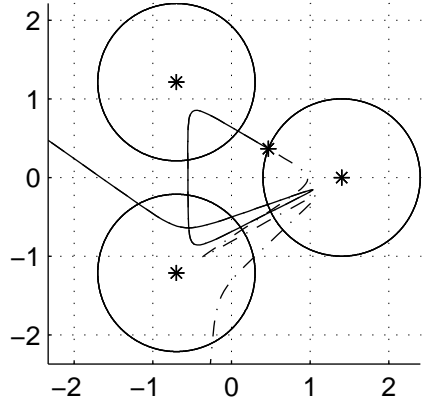


Figure 5: A typical trajectory: Stars mark the potential centers. In this case, $R = 1.4$ and $E = 0.5$. The circles drawn in the figure have radius 1, and the disjoint union of their cotangent bundles form the Poincaré section. Trajectories start on the circle centered at bump 0 (the bumps are, counterclockwise, 0, 1, and 2) with some given angle θ and angular momentum p_θ . This trajectory generates the finite sequence $(\dot{0}, 1, 2, 0, 2, \infty)$. (Symbolic sequences are discussed later in the paper.) An illustration of resonance computation is depicted in Figure 4. The dashed line is the time-reversed trajectory with the same initial conditions, generating the sequence $(\infty, 2, 0, 2, \dot{0})$.

¹³That is, $D(A \cup B) = \max(D(A), D(B))$. For details, see [8].

to the dimension of the trapped set. More importantly, most trajectories which visit all three bumps will also cut through P .

One can thus reduce the dimension of the problem by restricting the flow to $K_E \cap P$, as follows: Take any point (θ, p_θ) in P_k , and form the corresponding point (x, y, p_x, p_y) in R^4 via Equation (43). Follow along the trajectory $\Phi_t(x, y, p_x, p_y)$. If the trajectory does not escape, eventually it must encounter one of the other circles, say $C_{k'}$. Generically, trajectories cross $C_{k'}$ twice at each encounter, and we denote the coordinates (θ', p'_θ) (in $P_{k'}$) of the *outgoing intersection* by

$$\tilde{\Phi}(\theta, p_\theta, k) = (\theta', p'_\theta, k'). \quad (45)$$

If a trajectory escapes from the trapping region, we can symbolically assign ∞ to $\tilde{\Phi}$. The map $\tilde{\Phi}$ then generates stroboscopic recordings of the flow Φ_t on the submanifold P , and the corresponding discrete dynamical system has trapped set $K_E \cap P$. So, instead of computing Φ_t on R^4 , one only needs to compute $\tilde{\Phi}$ on P . By symmetry, it will suffice to compute the dimension of $\tilde{K}_E = K_E \cap P_0$. Pushing \tilde{K}_E forward along the flow Φ_t adds one dimension, so $D(K_E) = D(\tilde{K}_E) + 1$. Being a subset of the two-dimensional space P_0 , \tilde{K}_E is easier to work with.

Readers interested in a more detailed discussion of Poincaré sections and their use in dynamics are referred to [29]. For an application to the similar but simpler setting of hard disc scattering, see [9, 12]. Also, Knauf has applied some of these ideas in a theoretical investigation of classical scattering by Coulombic potentials [17].

5.2 Self-Similarity

Much is known about the self-similar structure of the trapped set for hard disc scattering [9, 12]; less is known about “soft scatterers” like the triple gaussian system. However, computational results and analogy with hard disc scattering give strong support to the idea that K (and hence \tilde{K}_E) is self-similar.¹⁴ Consider Figures 6 - 12: They show clearly that \tilde{K}_E is self-similar. (In these images, $E = 0.5$ and $R_0 = 1.0$.) However, it is also clear that, unlike objects such as the Cantor set or the Sierpiński gasket, \tilde{K}_E is not exactly self-similar.

5.3 Symbolic Dynamics

The computation of $D(\tilde{K}_E)$ uses symbolic sequences, which requires a brief explanation: For any point (θ, p_θ) , let s_i denote the third component of $\tilde{\Phi}^i(\theta, p_\theta)$ (see (45)), for any integer i . Thus, s_i is the index k of the circle

¹⁴More precisely, *self-affine*.

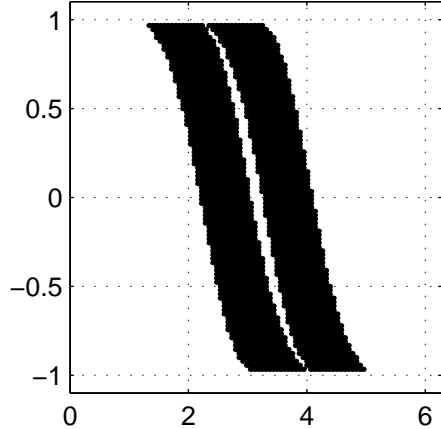


Figure 6: Points in P_0 which do not go to ∞ after one iteration of $\tilde{\Phi}$. The horizontal axis is θ and the vertical axis is p_θ .

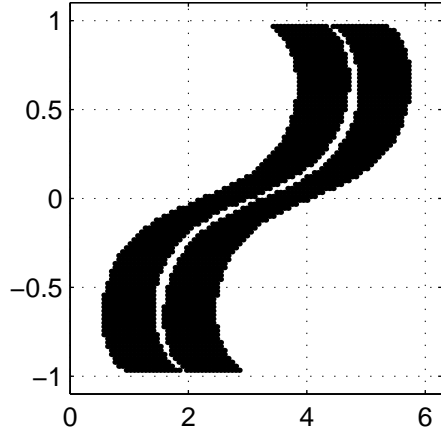


Figure 7: Points in P_0 which do not go to ∞ after one iteration of $\tilde{\Phi}^{-1}$. The horizontal axis is θ and the vertical axis is p_θ .

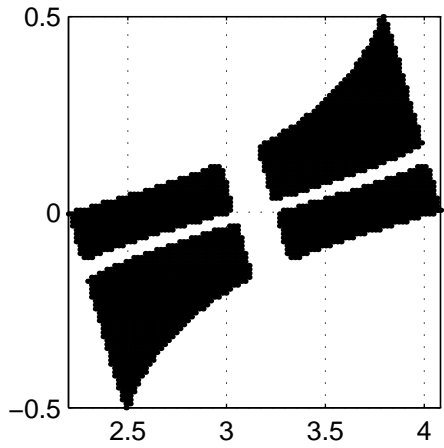


Figure 8: The intersection of the sets in Figures 6 and 7. These points correspond to symmetric sequences of length 3.

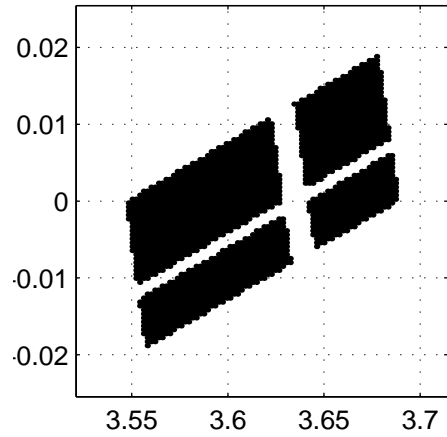


Figure 10: The cut-out part of Figure 9, magnified. Recall that these correspond to symmetric sequences of length 5; compare with Figure 8.

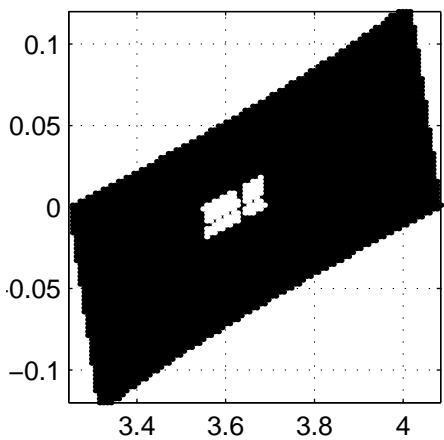


Figure 9: The lower-right “island” in Figure 8, magnified. The white cut-out in the middle is the subset corresponding to symmetric sequences of length 5.

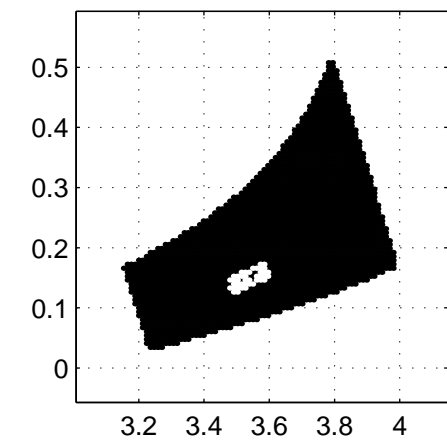


Figure 11: The upper-right island in Figure 8. The white cut-out in the middle is, again, the subset corresponding to symmetric sequences of length 5.

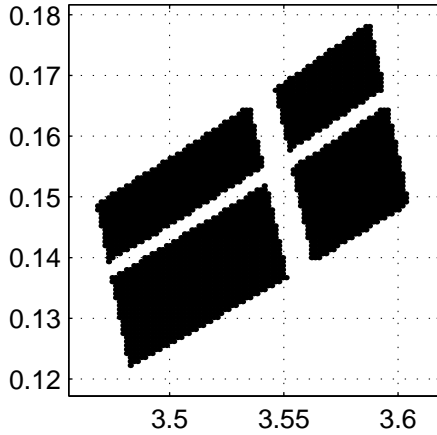


Figure 12: The cut-out part of Figure 11, magnified. Recall that these correspond to symmetric sequences of length 5. Compare with Figures 8 and 10.

C_k that the trajectory intersects at the i th iteration of $\tilde{\Phi}$ (or the $|i|$ th iteration of $\tilde{\Phi}^{-1}$). Such symbolic sequences $s = (\dots s_i, s_{i+1} \dots)$ satisfy $s_i \in \{0, 1, 2, \infty\}$ and $s_i \neq s_{i+1}$ for all i , and with ∞ occurring only at the ends. Let us call sequences satisfying these conditions *valid*.

For example, the trajectory in Figure 4 generates the valid sequence $(\dot{0}, 1, 2, 0, 2, \infty)$, where the dot over 0 indicates that the initial point (θ, p_θ) of the trajectory belongs to P_0 . Thus, we can label collections of trajectories using valid sequences, and label points in P with “dotted” sequences. Clearly, trapped trajectories generate bi-infinite sequences.¹⁵

The islands in Figures 8 - 11 correspond to *symmetric sequences centered at 0*, of the form $s = (\dots s_{-k}, \dots, s_{-1}, \dot{0}, s_1, s_2, \dots, s_k \dots)$: By keeping track of the symbolic sequences generated by each trajectory, one can easily label and isolate each island. This is a useful property from the computational point of view.

5.4 Dimension Estimates

To compute the Minkowski dimension using Equation (13), we need to determine when a given point is within ϵ of \tilde{K}_E . This is generally impossible: The best one can do is to generate longer and longer trajectories which stay trapped for increasing (but finite) amounts of time.

Instead, one can estimate a closely related quantity, the *information dimension*, in the following way: Let $\tilde{K}_E^{(k)}$

¹⁵In hard disc scattering, the converse holds for sufficiently large R : To each bi-infinite valid sequence there exists a trapped trajectory generating that sequence. This may not hold in the triple gaussian model, and in any case it is not necessary for the computation.

denote the set of all points in P_0 corresponding to symmetric sequences of length $2k + 1$ centered at 0. That is, $\tilde{K}_E^{(k)}$ consists of all points in P_0 which generate trajectories (both forwards and backwards in time) that bounce at least k times before escaping. The sets $\tilde{K}_E^{(k)}$ decrease monotonically to \tilde{K}_E : $\tilde{K}_E^{(k)} \supset \tilde{K}_E^{(k+1)}$ and $\cap_{k=0}^{\infty} \tilde{K}_E^{(k)} = \tilde{K}_E$.

One can then estimate the information dimension using the following algorithm:

1. *Initialization*: Cover P_0 with a mesh L_0 with $N_0 \times N_0$ grid points and mesh size ϵ_0 .
2. *Recursion*: Begin with $\tilde{K}_E^{(1)}$, which consists of four islands corresponding to symmetric sequences of length $2 \cdot 1 + 1 = 3$ (see Figure 8). Magnify each of these islands and compute the sub-islands corresponding to symmetric sequences of length 5 (see Figures 9 and 11). Repeat this procedure to recursively compute the islands of $\tilde{K}_E^{(k+1)}$ from those of $\tilde{K}_E^{(k)}$. Continue until $k = k_0$, where k_0 is sufficiently large that each island of $\tilde{K}_E^{(k_0)}$ has diameter smaller than the mesh size ϵ_0 of L_0 .
3. *Estimation*: Using the islands of $\tilde{K}_E^{(k_0)}$, estimate the probability

$$p_{ij} = \frac{\text{vol}(\tilde{K}_E^{(k_0)} \cap B_{ij})}{\text{vol}(\tilde{K}_E^{(k_0)})} \quad (46)$$

for the (ij) th cell of L_0 . We can then compute the dimension via

$$D(\tilde{K}_E) \approx \frac{-\sum_{ij} p_{ij} \log(p_{ij})}{\log(N_0)}, \quad (47)$$

which reduces to (13) when the distribution is uniform because $\epsilon_0 \sim 1/N_0$.

Under suitable conditions (as is assumed to be the case here), the information dimension agrees with both the Hausdorff and the Minkowski dimensions.¹⁶

The algorithm begins with the lattice L_0 with which one wishes to compute the dimension. It then recursively computes $\tilde{K}_E^{(k)}$ for increasing values of k , until it closely approximates \tilde{K}_E relative to the mesh size of L_0 . It is easy to keep track of points belonging to each island in this computation, since each island corresponds uniquely to a finite symmetric sequence. Note that while the large mesh L_0 remains fixed throughout the computation, the recursive steps require smaller $N_1 \times N_1$ meshes around each island of $\tilde{K}_E^{(k)}$ up to the value of k specified by the algorithm. See Figure 13.

¹⁶See [23] for a discussion of the relationship between these dimensions, as well as their use in multifractal theory.

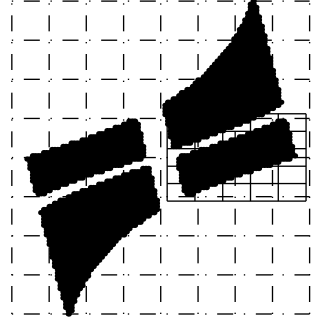


Figure 13: This figure illustrates the recursive step in the dimension estimation algorithm: The dashed lines represent L_0 , while the solid lines represent a smaller mesh centered on one of the islands. The $N_0 \times N_0$ mesh L_0 remains fixed throughout the computation, but the smaller $N_1 \times N_1$ mesh is constructed for each island of $\tilde{K}_E^{(k)}$ up to the value of k specified by the algorithm.

6 Numerical Results

6.1 Resonance Counting

As an illustration of complex scaling, Figures 14 - 18 contain resonances for $R = 1.4$ and $\hbar \in [0.017, 0.025]$. Eigenvalues of $\hat{H}_{N,\alpha}$ for different values of α are marked by different styles of points, and the box has depth \hbar and width 0.2, with $E_0 = 0.4$ and $E_1 = 0.6$. These plots may seem somewhat empty because only those eigenvalues of $\hat{H}_{N,\alpha}$ in regions of interest were computed. Notice the cluster of eigenvalues near the bottom edge of the plots: These are *not* resonances because they vary under perturbations in α . Instead, they belong to an approximation of the (scaled) continuous spectrum.

It is more interesting to see $\log(N_{res})$ as a function of $-\log(\hbar)$ and R . This is shown in Figures 19 and 20. Using least-squares regression, we can extract approximate slopes for the curves in Figure 19; these are shown in Table 2 and plotted in Figure 21.

6.2 Trapped Set Dimension

For comparison, $\frac{D(K_E)+1}{2}$ is plotted as a function of R in Figure 22. The figure contains curves corresponding to different energies E : The top curve corresponds to $E = 0.4$, the middle curve $E = 0.5$, and the bottom curve $E = 0.6$. It also contains curves corresponding to dif-

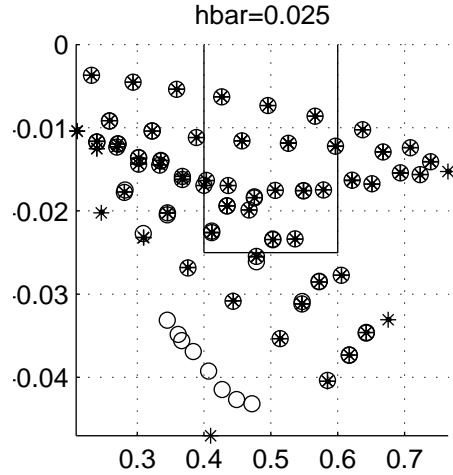


Figure 14: These are the eigenvalues of $\hat{H}_{N,\alpha}$, for $E = 0.5$, $\hbar = 0.025$, $R = 1.4$, and $\alpha \in \{0.0624, 0.0799, 0.0973\}$. This calculation used an 102×108 grid, and 90 out of $N = 11016$ eigenvalues were computed.

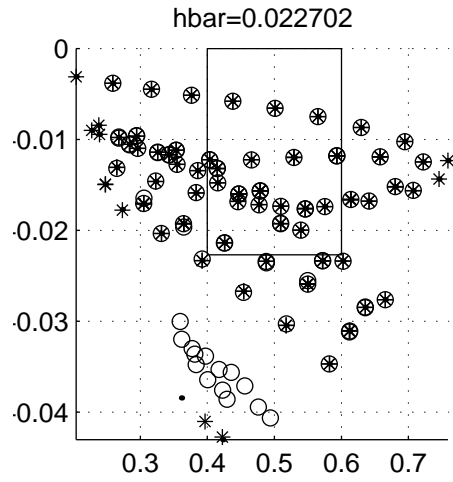


Figure 15: Eigenvalues for $E = 0.5$, $\hbar = 0.022702$, $R = 1.4$, and $\alpha \in \{0.0567, 0.0741, 0.0916\}$, using 112×119 grid and 98 out of $N = 13328$ eigenvalues.

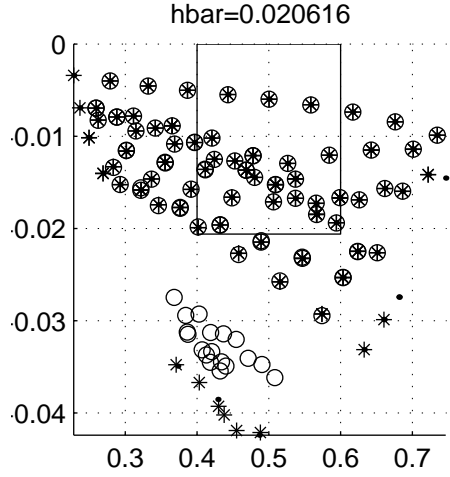


Figure 16: Eigenvalues for $E = 0.5$, $\hbar = 0.020616$, $R = 1.4$, and $\alpha \in \{0.0515, 0.0689, 0.0864\}$, using 123×131 grid and 107 out of $N = 16113$ eigenvalues.

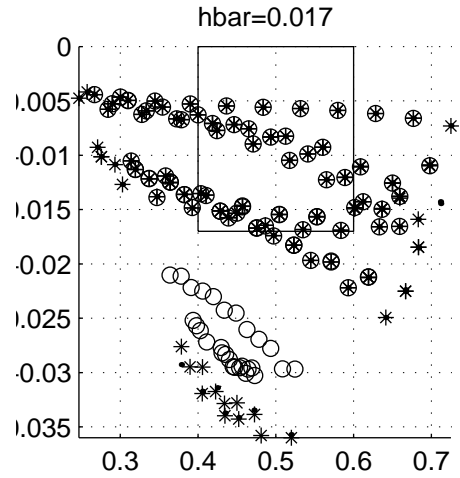


Figure 18: Eigenvalues for $E = 0.5$, $\hbar = 0.017$, $R = 1.4$, and $\alpha \in \{0.0425, 0.0599, 0.0774\}$, using 149×159 grid and 127 out of $N = 23691$ eigenvalues.

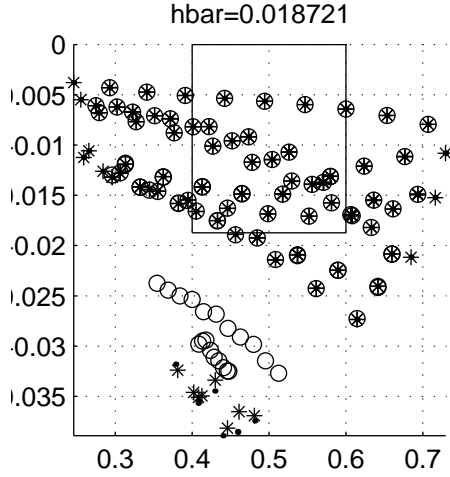


Figure 17: Eigenvalues for $E = 0.5$, $\hbar = 0.018721$, $R = 1.4$, and $\alpha \in \{0.0468, 0.0642, 0.0817\}$, using 135×144 grid and 116 out of $N = 19440$.

R	$E = 0.4$	$E = 0.5$	$E = 0.6$
1.4	1.3092	1.2885	1.261
1.45	1.3084	1.2834	1.2558
1.5	1.3037	1.2829	1.2497
1.55	1.3007	1.2773	1.2521
1.6	1.2986	1.2725	1.2511
1.65	1.2912	1.2694	1.2488
1.7	1.2893	1.2636	1.2524

Table 1: Estimates of $\frac{D(K_E)+1}{2}$ as a function of R .

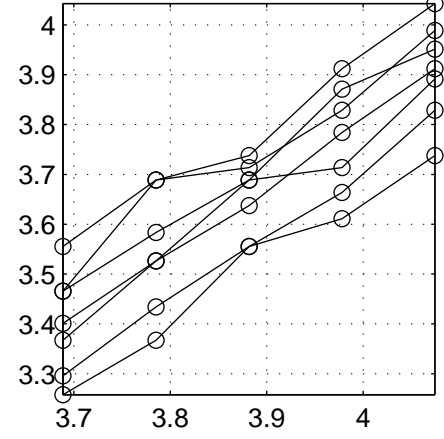


Figure 19: $\log(N_{res})$ as a function of $-\log(\hbar)$, for \hbar varying from 0.017 to 0.025 and $R = 1.4 + 0.05 \cdot k$, with $0 \leq k \leq 6$. (The lowest curve corresponds to $R = 1.7$, while the highest curve corresponds to $R = 1.4$.)

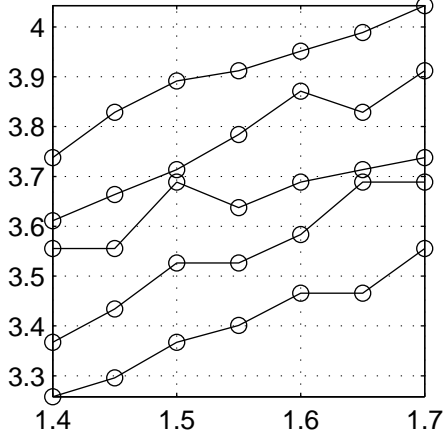


Figure 20: $\log(N_{res})$ as a function of R , for different values of $-\log(\hbar)$: The highest curve corresponds to $\hbar = 0.017$, while the lowest curve corresponds to $\hbar = 0.025$.

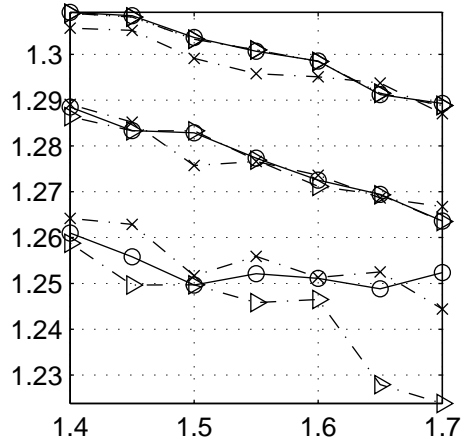


Figure 22: This figure shows $\frac{D(K_E)+1}{2}$ as a function of R : The top group of curves have $E = 0.4$, the middle $E = 0.5$, and the bottom $E = 0.6$. Solid curves marked with circles represent computations where $N_0 = 10000$, $N_1 = 100$, $\frac{2\pi}{3} \leq \theta \leq \frac{4\pi}{3}$, and $-\frac{1}{2} \leq p_\theta \leq \frac{1}{2}$. Dashed curves marked with X's represent computations where $N_0 = 14142$, whereas dashed curves marked with triangles represent computations where $N_0 = 10000$ and $N_1 = 71$. The recursion depth k_0 in all these figures is 6. The $E = 0.6$ curve does not appear to have completely converged but suffices for our purpose here.

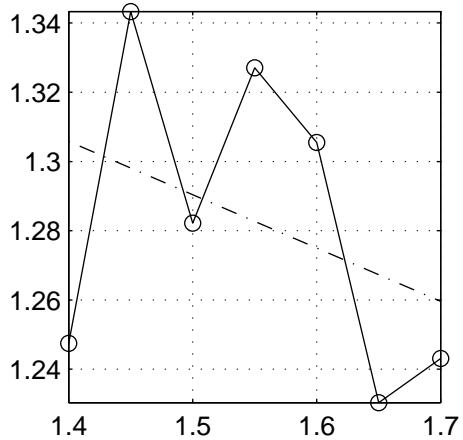


Figure 21: The slopes extracted from Figure 19, as a function of R . The dotted curve is a least-squares regression of the “noisy” curve.

R	slope	$\frac{D(K_E)+1}{2}$	relative error
1.4	1.2475	1.2885	0.032888
1.45	1.3433	1.2834	0.044645
1.5	1.2822	1.2829	0.00052244
1.55	1.327	1.2773	0.037472
1.6	1.3055	1.2725	0.025256
1.65	1.2304	1.2694	0.031756
1.7	1.2431	1.2636	0.016509

Table 2: This table shows the slopes extracted from Figure 19, as well as the scaling exponents one would expect if the conjecture were true ($(D(K_E) + 1)/2$, computed at $E = 0.5$). Relative errors are also shown.

ferent program parameters, to test the numerical convergence of dimension estimates. These curves were computed with $\theta \in [\frac{2\pi}{3}, \frac{4\pi}{3}]$, $p_\theta \in [-\frac{1}{2}, \frac{1}{2}]$, and recursion depth $k_0 = 6$ (corresponding to symmetric sequences of length $2 \cdot 6 + 1 = 13$); the caption contains the values of N_0 and N_1 for each curve. For reference, Table 1 contains the dimension estimates shown in the graph. It is important to note that, while the dimension does depend on E and R , it only does so weakly: Relative to its value, $\frac{D(K_E)+1}{2}$ is very roughly constant across the range of R and E computed here.

6.3 Discussion

Table 2 contains a comparison of $\frac{D(K_E)+1}{2}$ (for $E = 0.5$) as a function of R , versus the scaling exponents from Figure 21. Figure 23 is a graphical representation of similar information. This figure shows that even though the scaling curve in Figure 21 is noisy, its trend nevertheless agrees with the conjecture. Furthermore, the relative size of the fluctuations is small. At the present time, the source of the fluctuation is not known, but it is possibly due to the fact that the range of \hbar explored here is simply too large to exhibit the asymptotic behavior clearly.¹⁷

Figures 24 - 30 contain plots of $\log(N_{res})$ versus $-\log(\hbar)$, for various values of R . Along with the numerical data, the least-squares linear fit and the scaling law predicted by the conjecture are also plotted.¹⁸ In contrast with Figure 23, these show clear agreement between the asymptotic distribution of resonances and the scaling exponent predicted by the conjecture.

¹⁷But see Footnote 8.

¹⁸The conjecture only supplies the exponents for power laws, not the constant factors. In the context of these logarithmic plots, this means the conjecture gives us only the slopes, not the vertical shifts. It was thus necessary to compute an y -intercept for each “prediction” curve (for the scaling law predicted by the conjecture) using least squares.

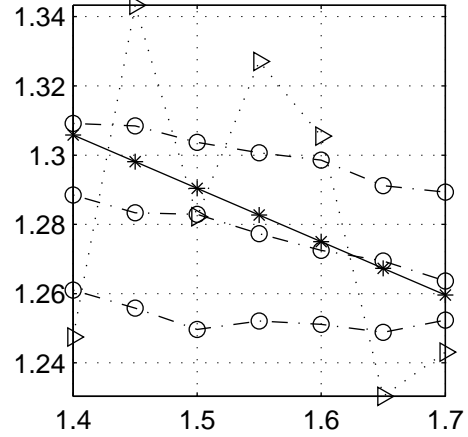


Figure 23: Dashed lines with circles represent $\frac{D(K_E)+1}{2}$ as functions of R , for $E \in \{0.4, 0.5, 0.6\}$. The dotted curve with triangles is the scaling exponent curve from Figure 21, while the solid curve with stars is the linear regression curve from that figure. Relative to the value of the dimension, the fluctuations are actually fairly small: See Table 2 for a quantitative comparison.

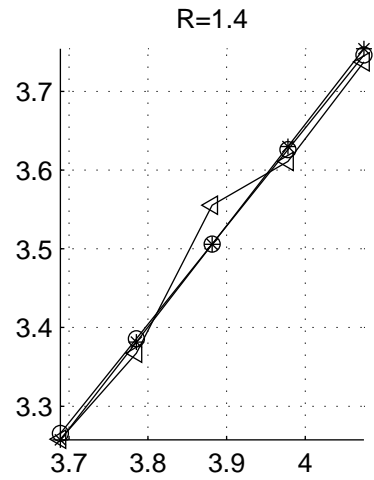


Figure 24: For $R = 1.4$: Triangles represent numerical data, circles least squares regression, and stars the slope predicted by the conjecture. \hbar ranges from 0.025 down to 0.017.

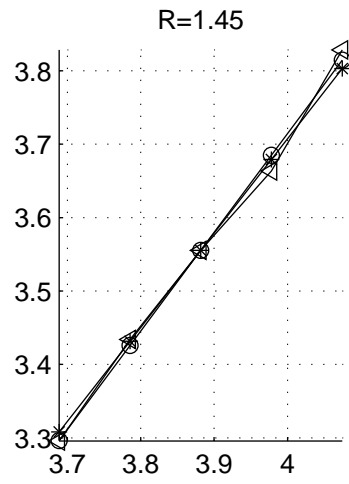


Figure 25: Same for $R = 1.45$. Again, \hbar ranges from 0.025 to 0.017.

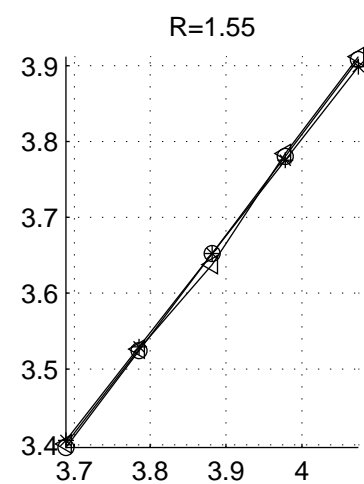


Figure 27: $R = 1.55$

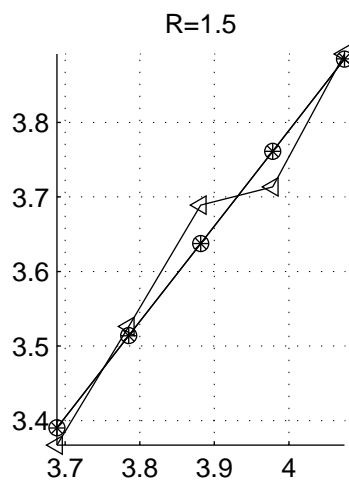


Figure 26: $R = 1.5$, $0.017 \leq \hbar \leq 0.025$.

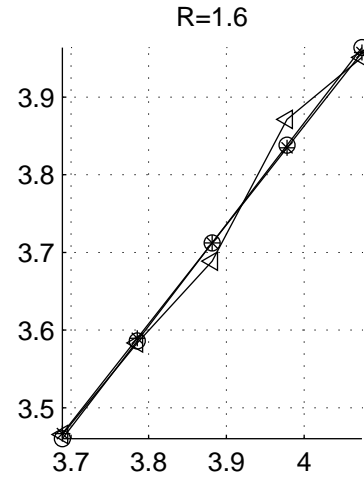


Figure 28: $R = 1.6$, $0.017 \leq \hbar \leq 0.025$.

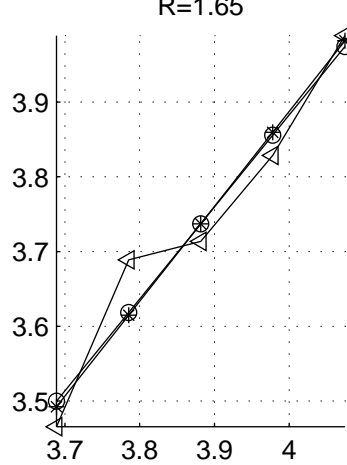


Figure 29: $R = 1.65$, $0.017 \leq \hbar \leq 0.025$.

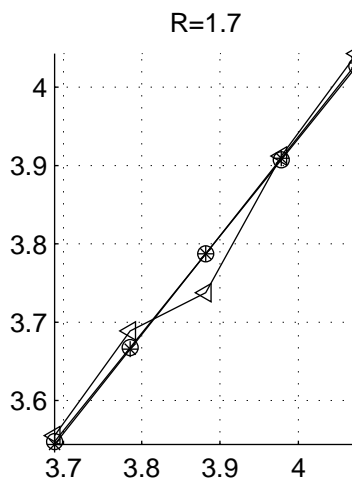


Figure 30: $R = 1.7$, $0.017 \leq \hbar \leq 0.025$.

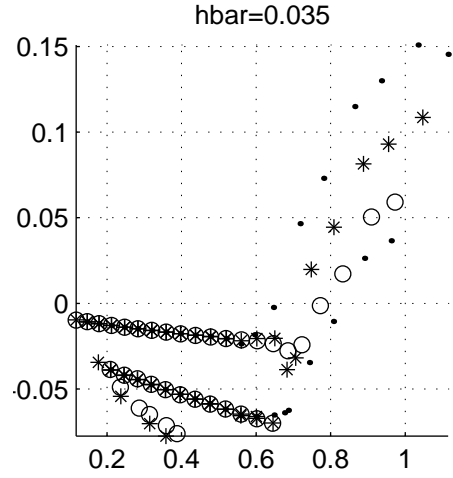


Figure 31: Resonances for two-bump scattering with $\hbar = 0.035$.

6.4 Double Gaussian Scattering

Finally, we compute resonances for the double gaussian model (setting $m = 2$ in (6)). This case is interesting for two reasons: First, there exist rigorous results [13, 21] against which we can check the correctness of our results. Second, it helps determine the validity of semiclassical arguments for the values of \hbar used in computing resonances for the triple gaussian model.

The resonances are shown in Figures 31 - 37: In these plots, $R = 1.4$ and \hbar ranges from 0.035 to 0.015. One can observe apparent pseudospectral effects in the first few figures [30, 36]; this is most likely because the scaling angle α used here is twice as large as suggested in Section 4.1, to exhibit the structure of resonances farther away from the real axis.

To compare this information with known results [13, 21], we need some definitions: For a given energy $0 < E < 1$, define $C(E)$ by

$$C(E) = 2 \int_{x_0(E)}^{x_1(E)} \sqrt{2 \cdot (E - V(x))} dx, \quad (48)$$

where the limits of integration are

$$\begin{aligned} x_0(E) &= -R + \sqrt{-2\sigma^2 \log(E)}, \\ x_1(E) &= R - \sqrt{-2\sigma^2 \log(E)}. \end{aligned} \quad (49)$$

Let $\theta(E)$ denote the larger (in absolute value) eigenvalue of $D\tilde{\Phi}(0, 0)$; $\log(\theta)$ is the Lyapunov exponent of $\tilde{\Phi}$, and is easy to compute numerically in this case. Note that for two-bump scattering, each energy E determines a unique periodic trapped trajectory, and $C(E)$ is the classical action computed along that trajectory.

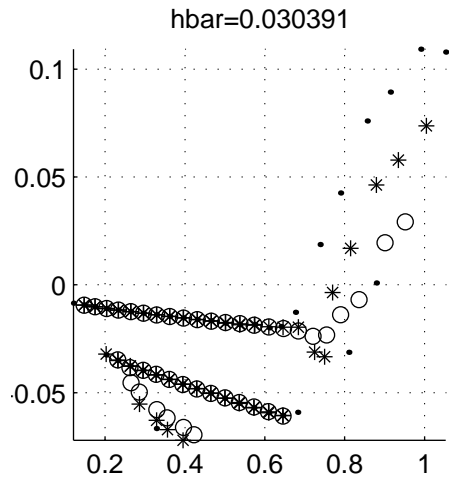


Figure 32: Resonances for two-bump scattering with $\hbar = 0.030391$.

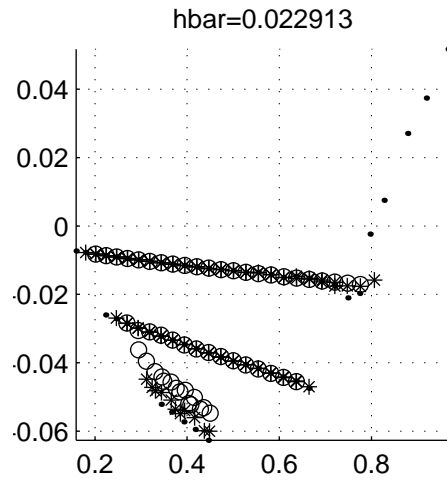


Figure 34: Resonances for two-bump scattering with $\hbar = 0.022913$.

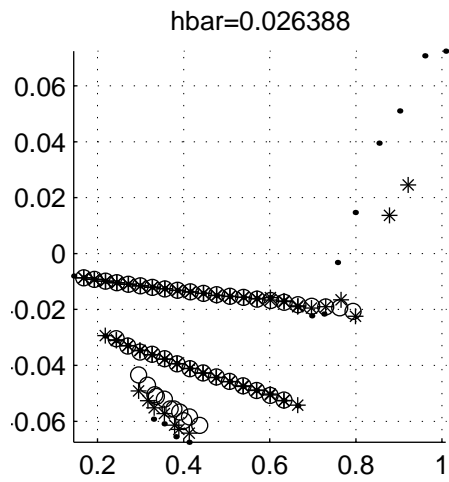


Figure 33: Resonances for two-bump scattering with $\hbar = 0.026388$.

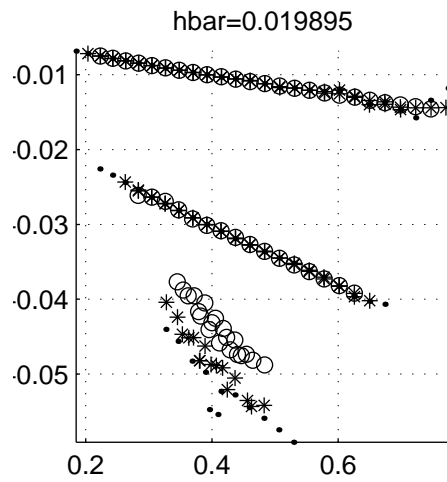


Figure 35: Resonances for two-bump scattering with $\hbar = 0.019895$.

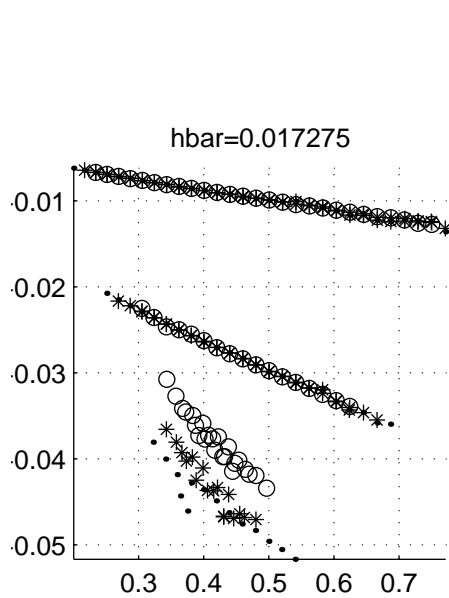


Figure 36: Resonances for two-bump scattering with $\hbar = 0.017275$.

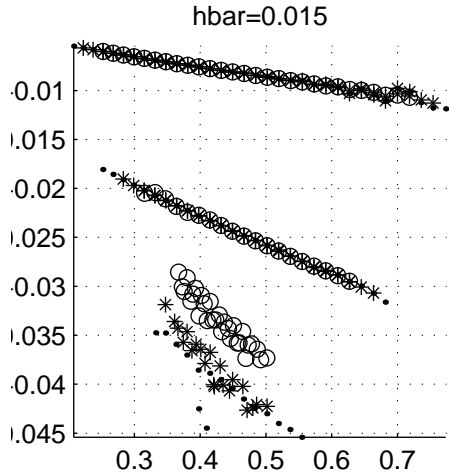


Figure 37: Resonances for two-bump scattering with $\hbar = 0.015$.

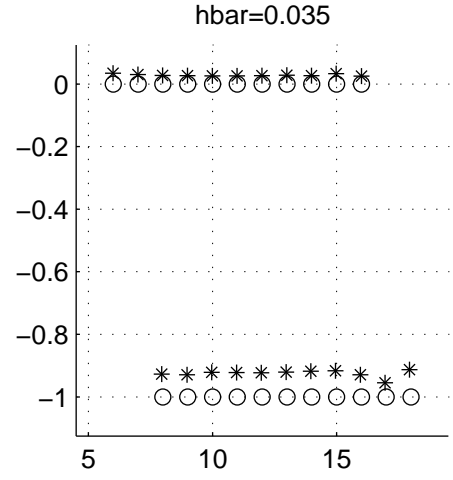


Figure 38: Lattice points for $\hbar = 0.035$.

Since these expressions are analytic, they have continuations to a neighborhood of the real line — $C(E)$ becomes a contour integral. In [13], it was shown that any resonance $\lambda = E - i\gamma$ must satisfy

$$C(\lambda) = 2\pi\hbar \left(m + \frac{1}{2} \right) - i\hbar \left(n + \frac{1}{2} \right) \log(\theta(Re(\lambda))) + O(\hbar^2), \quad (50)$$

where m and n are nonnegative integers. (The $\frac{1}{2}$ in $m + \frac{1}{2}$ comes from the Maslov index associated with the classical turning points.) This suggests that we define the map $F(\lambda) = (F_1(\lambda), F_2(\lambda))$, where

$$F_1(\lambda) = \frac{Re(C(\lambda))}{2\pi\hbar} - \frac{1}{2} \quad (51)$$

and

$$F_2(\lambda) = \frac{Im(C(\lambda))}{\hbar \log(\theta(Re(\lambda)))} + \frac{1}{2}. \quad (52)$$

F should map resonances to points on the square integer lattice, and this is indeed the case: Figures 38 - 44 contain images of resonances under F , with circles marking the nearest lattice points. The agreement is quite good, in view of the fact that we neglected terms of order \hbar^2 in Equation (50).

7 Conclusions

Using standard numerical techniques, one can compute a sufficiently large number of resonances for the triple gaussian system to verify their asymptotic distribution in the semiclassical limit $\hbar \rightarrow 0$. This, combined with effective estimates of the fractal dimension of the classical trapped

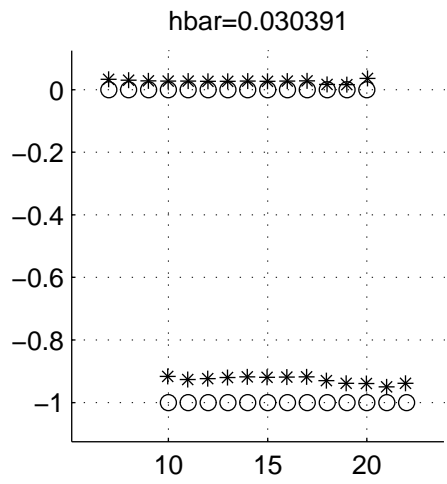


Figure 39: Lattice points for $\hbar = 0.030391$.

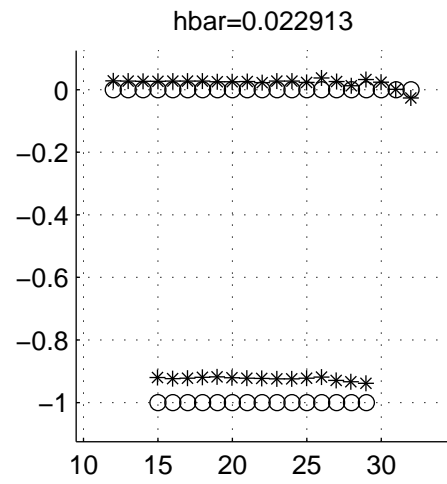


Figure 41: Lattice points for $\hbar = 0.022913$.

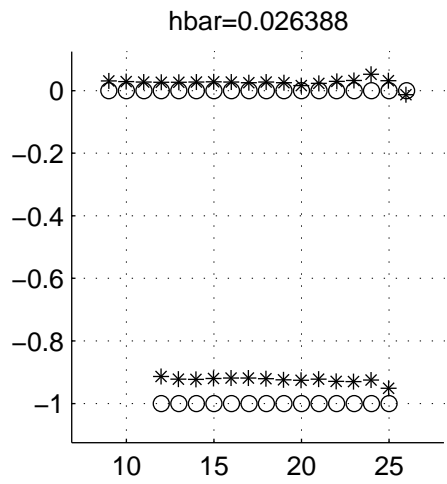


Figure 40: Lattice points for $\hbar = 0.026388$.

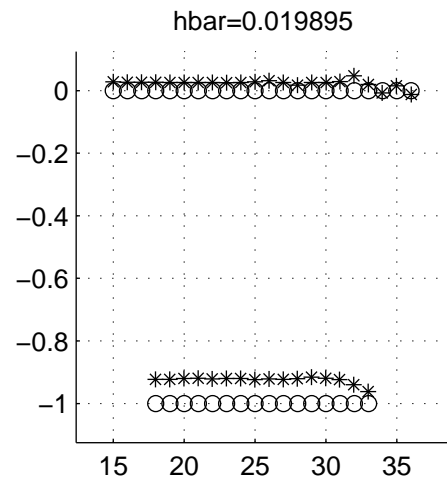


Figure 42: Lattice points for $\hbar = 0.019895$.

set, gives strong evidence that the number of resonances N_{res} in a box $[E_0, E_1] - i[0, \hbar]$, for sufficiently small $|E_1 - E_0|$ and \hbar ,

$$N_{res} \sim \hbar^{-\frac{D(K_E)+1}{2}}, \quad (53)$$

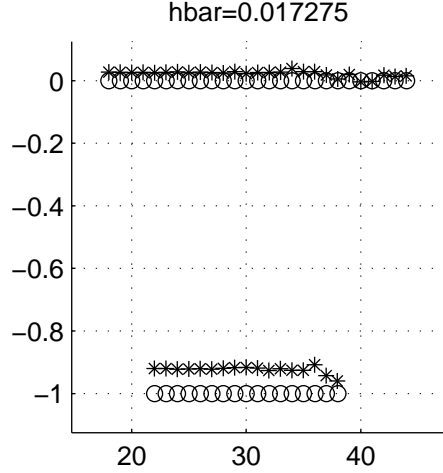


Figure 43: Lattice points for $\hbar = 0.017275$.

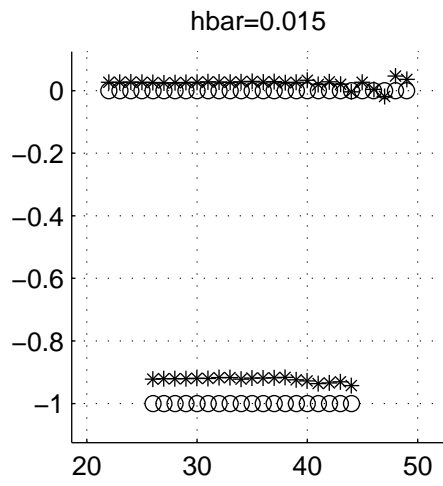


Figure 44: Lattice points for $\hbar = 0.015$.

as one can see in Figure 23 and Table 2. Furthermore, the same techniques, when applied to double gaussian scattering, produce results which agree with rigorous semiclassical results. This supports the correctness of our algorithms and the validity of semiclassical arguments for the range of \hbar explored in the triple gaussian model. The computation also hints at more detailed structures in the distribution of resonances: In Figures 14 - 18, one can clearly see gaps and strips in the distribution of resonances. A complete understanding of this structure requires further investigation.

While we do not have rigorous error bounds for the dimension estimates, the numerical results are convincing. It seems, then, that the primary cause for our failure to observe the conjecture in a “clean” way is partly due to the size of \hbar : If one could study resonances at much smaller values of \hbar , the asymptotics may become more clear.

8 Acknowledgments

Thanks to J. Demmel and B. Parlett for crucial help with matrix computations, and to X. S. Li and C. Yang for ARPACK help. Thanks are also due to R. Littlejohn and M. Cargo for their help with bases and matrix elements, and to F. Bonetto for suggesting a practical method for computing fractal dimensions. Many thanks to Z. Bai, W. H. Miller, and J. Harrison for helpful conversations, and to the Mathematics Department at Lawrence Berkeley National Laboratory for computational resources. Finally, the author owes much to M. Zworski for inspiring most of this work.

KL was supported by the Fannie and John Hertz Foundation.

References

- [1] J. Aguilar, J. M. Combes. “A class of analytic perturbations for one body Schrödinger Hamiltonians,” *Comm. Math. Phys.* **22** (1971), 269-279.
- [2] E. Anderson, Z. Bai, C. Bischof, et al. *LAPACK User’s Guide, Third Edition*. SIAM, 1999.
- [3] E. Balslev, J. M. Combes. “Spectral properties of many-body Schrödinger operators with dilation analytic interactions,” *Comm. Math. Phys.* **22** (1971), 280-294.

- [4] R. Barrett, M. Berry, T. F. Chan, *et al.* *Templates for the Solution of Linear Systems: Building Blocks for Iterative Methods*. SIAM, 1994.
- [5] H. A. Bethe, E. E. Salpeter. *Quantum Mechanics of One- and Two-Electron Atoms*. Plenum Publications, c1977.
- [6] M. J. Davis, E. J. Heller. “Semiclassical Gaussian basis set method for molecular vibrational wave functions,” *J. Chem. Phys.* **71** (1979), no. 8, 3383.
- [7] M. Dimassi, J. Sjöstrand. *Spectral Asymptotics in the Semi-Classical Limit*. Cambridge University Press, 1999.
- [8] K. J. Falconer. *Fractal Geometry: Mathematical Foundations and Applications*. John Wiley and Sons, 1990.
- [9] P. Gaspard, S. A. Rice. “Scattering from a classically chaotic repellor,” *J. Chem. Phys.* **90** (1989), 2225.
- [10] P. Gaspard, S. A. Rice. “Semiclassical quantization of the scattering from a classically chaotic repellor,” *J. Chem. Phys.* **90** (1989), 2242.
- [11] P. Gaspard, S. A. Rice. “Exact quantization of the scattering from a classically chaotic repellor,” *J. Chem. Phys.* **90** (1989), 2255.
- [12] P. Gaspard. *Chaos, Scattering, and Statistical Mechanics*. Cambridge University Press, 1998.
- [13] C. Gérard, J. Sjöstrand. “Semiclassical resonances generated by a closed trajectory of hyperbolic type,” *Comm. Math. Phys.* **108** (1987), no. 3, 391-421.
- [14] L. Guillopé, M. Zworski. “Wave trace for Riemann surfaces,” *Geom. and Func. Anal.* **6** (1999), 1156-1168.
- [15] I. P. Hamilton, J. C. Light. “On distributed Gaussian bases for simple model multidimensional vibrational problems,” *J. Chem. Phys.* **84** (1986), no. 1, 306.
- [16] M. Kac. “Can one hear the shape of a drum?” *Amer. Math. Monthly* **73** (1966), no. 4, 1-23.
- [17] A. Knauf. “The n -Centre Problem of Celestial Mechanics” (2000), preprint.
- [18] A. Lahmar-Benbernou, A. Martinez. “On Helffer-Sjöstrand’s theory of resonances,” preprint.
- [19] R. B. Lehoucq, D. C. Sorensen, C. Yang. *ARPACK User’s Guide: Solution of Large-Scale Eigenvalue Problems with Implicitly Restarted Arnoldi Methods*. SIAM, 1998.
- [20] J. C. Light, I. P. Hamilton, J. V. Lill. “Generalized discrete variable approximation in quantum mechanics,” *J. Chem. Phys.* **82** (1985), 1400-1409.
- [21] W. H. Miller. “Classical-limit Green’s function (fixed-energy propagator) and classical quantization of nonseparable systems,” *J. Chem. Phys.* **56** (1972), no. 1, 38-45.
- [22] W. H. Miller. “Tunneling and state specificity in unimolecular reactions,” *Chem. Rev.* **87** (1987), 19-27.
- [23] Ya. B. Pesin. *Dimension Theory in Dynamical Systems: Contemporary Views and Applications*. Univ. of Chicago Press, 1997.
- [24] T. N. Rescigno, M. Baertschy, W. A. Isaacs, C. W. McCurdy. “Collisional breakup in a quantum system of three charged particles,” *Science* **286** (1999), 2474-2479.
- [25] W. McC. Siebert. *Circuits, Signals, and Systems*. MIT Press, 1986.
- [26] B. Simon. “The definition of molecular resonance curves by the method of exterior complex scaling,” *Phys. Lett. A* **71** (1979), 211-214.
- [27] J. Sjöstrand. “Geometric bounds on the density of resonances for semi-classical problems,” *Duke Math. J.* **60** (1990), 1-57.
- [28] J. Sjöstrand, M. Zworski. “Complex scaling and the distribution of scattering poles,” *Jour. Amer. Math. Soc.* **4** (1991), 729-769.
- [29] G. J. Sussman, J. Wisdom, M. E. Mayer. *Structure and Interpretation of Classical Mechanics*. MIT Press, 2001.
- [30] L. N. Trefethen. “Pseudospectra of Linear Operators,” *SIAM Review* **39** (1989), no. 3, 383-406.
- [31] B. A. Waite, W. H. Miller. “Model studies of mode specificity in unimolecular reaction dynamics,” *J. Chem. Phys.* **73** (1980), no. 8, 3713-3721.
- [32] B. A. Waite, W. H. Miller. “Mode specificity in unimolecular reaction dynamics: the Hénon-Heiles potential energy surface,” *J. Chem. Phys.* **74** (1981), no. 7, 3910-3915.

- [33] M. Wei, G. Majda, W. Strauss. “Numerical Computation of the Scattering Frequencies for Acoustic Wave Equations,” *J. Comp. Phys.* **75** (1988), no. 2, 345-358.
- [34] A. Wirzba. “Quantum mechanics and semiclassics of hyperbolic n -disk scattering systems,” *Phys. Rep.* **309** (1999), no. 1-2.
- [35] M. Zworski, “Dimension of the limit set and the density of resonances for convex co-compact hyperbolic surfaces,” *Invent. Math.* **136** (1999), 353-409.
- [36] M. Zworski, “Numerical linear algebra and solvability of partial differential equations” (2001), preprint.
- [37] M. Zworski. “Resonances in Geometry and Physics,” *Notices of the AMS*, March 1999, 319-328.